Hindawi
Mathematical Problems in Engineering
Volume 2020, Article ID 7418719, 14 pages
https://doi.org/10.1155/2020/7418719

Research Article

Research on Ceramic Spindle Loss Based on Ceramic Reverse Magnetic Effect

Ke Zhang, Zinan Wang, Xiaotian Bai, Huaitao Shi, and Songhua Li

School of Mechanical Engineering, Shenyang Jianzhu University, Shenyang 110168, China

Correspondence should be addressed to Zinan Wang; wzn1404589743@126.com

Received 31 July 2019; Revised 19 January 2020; Accepted 18 February 2020; Published 20 March 2020

Academic Editor: Luis M. López-Ochoa

Ceramic motorized spindle is a multifield, nonlinear, and strong coupling system. The present model ignores the reverse magnetic effect and has a poor accuracy on the loss of the spindle system. In the paper, Park transformation was used to establish the electromagnetic physical model of ceramic motorized spindle. By combining with the Jiles–Atherton theory, an eccentric magnetization model of a ceramic motorized spindle considering reverse magnetic properties was established. Energy consumption parameters were calculated under various working conditions. The influence of ceramic reverse magnetic characteristics on the motorized spindle loss was analyzed and verified by experiments. The results show that the simulation of the ceramic motorized spindle loss model is in good agreement with the experimental results. Compared with the experimental results, the average loss error was 2.1%. Due to the reverse magnetic characteristics, the application of ceramic motorized spindle can help reduce the system loss. The ceramic motorized spindle model provides a theoretical basis for the development of ceramic spindle energy loss and efficiency.

1. Introduction

As the core component of computerized numerical control (CNC) machine tools, the high-speed motorized spindle has a complex coupling system. Due to the reverse magnetic properties, the ceramic motorized spindle can work better under some special conditions, such as the nonmagnetic field of petrochemical and strong chemical corrosion environment [1–3]. Energy development and management are crucial to further improve the machining efficiency of motorized spindles in high-speed operation [4, 5]. Scholars have undertaken a significant amount of research. Many smart energy management algorithms are presented through Newton–Raphson and event-triggered-based distributed [6, 7]. In general, some loss minimization algorithms are proposed, which can predict the load torque and loss of induction motor. However, the effect of torque variations on efficiency was not deeply analyzed in higher order harmonic environments [8, 9]. Ismagilov et al. [10]calculated the loss of the high-speed spindle stator yoke. Wang et al. [11] established a novel small-signal model based on the characteristic equation, which can assess the system low-frequency stability, but the field of rotor magnetic density was not studied.

The common methods in motor are generally researched through air-gap flux density distribution, but in the spindle working process, the eccentric effect of the air gap was not considered [12, 13]. Some researchers [14–16] proposed a dynamic adjustable induction motor (AIM) considering the rotor skin effect on current, which improved the energy efficiency of the manufacturing process. However, in some cases, energy efficiency did not increase significantly in a large-load situation. Other researchers reported that harmonic had great impact on the magnitude of current. However, the reverse magnetic properties of the rotating shaft materials were not taken into account [17–19]. Many researchers [20–23] proposed some new energy-saving management, which can enhance efficiency through optimizing the motor current and torque, but the research studies did not involve a better fit for the ceramic spindle in some special cases. Nowadays, little investigation has been conducted to improve the loss, harmonics, efficiency, energy management, and other aspects of the spindle. Therefore, it is essential to pay enough attention to the magnetic field and energy loss of the ceramic motorized spindle.

In this paper, a general electromagnetic coupling model is established, which is suitable for a ceramic motorized spindle. The model takes into account the characteristics of the ceramic reverse magnetic effect. According to Park transformation, considering the deep analysis of magnetic field, the motor model of the ceramic motorized spindle is established. Based on the Jiles–Atherton theory, the mutual influence between the air gap, magnetic density, and loss of the ceramic motorized spindle is analyzed under different working conditions. The loss model of the ceramic motorized spindle is studied, revealing the relationship between reverse magnetic, harmonics, and loss. The electromagnetic model of the ceramic motorized spindle has high accuracy, which has been verified by experiments. A ceramic motorized spindle is of great significance to improve the energy output performance and reduce loss in extreme environments.

2. Electromagnetic Model of a Ceramic Motorized Spindle

2.1. Mechanism Model of a Ceramic Motorized Spindle. A ceramic motorized spindle directly connects induction motor with spindle. Driven by electromagnetic torque through an inverter, the ceramic spindle can rotate at high speed. It is a complex mixed system. There are complex electromagnetic coupling relationships in the ceramic motorized spindle. The shaft of the motorized spindle is made of a ceramic material. When the motorized spindle rotor rotates, the stator and rotor are magnetically connected. According to Faraday's law of electromagnetic induction, the mathematical model of magnetic flux is established. The internal space vector of the motorized spindle is shown in Figure 1(a). The axis of rotation and space complex plane are represented by complex coordinate. The axis of winding is served as the real space reference axis. G is the movement trajectory of space trajectory r. The motorized spindle vector parameters of space trajectory, real axis, and imaginary axis are shown as follows:

$$\begin{cases} \theta_{\mathrm{r}} = \displaystyle\int_0^t \omega_r dt, \\ r = R\cos\theta_{\mathrm{r}} + jR\sin\theta_{\mathrm{r}} = a + jb, \end{cases} \tag{1}$$

where θ_{r} is the electrical angle of the space vector and R is the amplitude of the space vector.

The relationship between current and the space vector in stationary and rotating axes is shown in Figure 1(b). The rotating magnetic field is generated by three-phase windings with high-speed rotation. The stator and rotor are projected into d and q axes through Park transformation. Park transformation can reduce the variables between electromagnetic parameters. The three-phase motor model of the motorized spindle is converted into a two-phase α and β static coordinate system and a two-phase d and q rotating coordinate system. The two-phase α and β stationary coordinate system rotates at ω angular velocity. The angle θ of rotor and stator flux direction is relative to the slip ratio s. A backward angle allows the flux to produce a constant current. According to Figure 1(b), the transformation relationship between the current's changes in coordinate axes can be obtained by applying Park transformation, as shown in the following equation [24]:

$$\begin{cases} i_\alpha = i_d\cos\theta - i_q\sin\theta, \\ i_\beta = i_d\sin\theta + i_q\cos\theta. \end{cases} \tag{2}$$

The relationship between flux and circuit in $dq0$ coordinates is shown in the following equation:

$$\begin{bmatrix} u_{ds} \\ u_{qs} \\ u_{0s} \end{bmatrix} = \begin{bmatrix} R_s & 0 & 0 \\ 0 & R_s & 0 \\ 0 & 0 & R_s \end{bmatrix} \begin{bmatrix} i_{ds} \\ i_{qs} \\ i_{0s} \end{bmatrix} + p \begin{bmatrix} \psi_{ds} \\ \psi_{qs} \\ \psi_{0s} \end{bmatrix} + \begin{bmatrix} -\omega\psi_{qs} \\ \omega\psi_{ds} \\ 0 \end{bmatrix},$$

$$\begin{bmatrix} u_{\mathrm{dr}} \\ u_{\mathrm{qr}} \\ u_{0r} \end{bmatrix} = \begin{bmatrix} R_r & 0 & 0 \\ 0 & R_r & 0 \\ 0 & 0 & R_r \end{bmatrix} \begin{bmatrix} i_{\mathrm{dr}} \\ i_{\mathrm{qr}} \\ i_{0r} \end{bmatrix} + p \begin{bmatrix} \psi_{\mathrm{dr}} \\ \psi_{\mathrm{qr}} \\ \psi_{0r} \end{bmatrix} + \begin{bmatrix} -(\omega - \omega_r)\psi_{\mathrm{qr}} \\ (\omega - \omega_r)\psi_{\mathrm{dr}} \\ 0 \end{bmatrix},$$

$$\begin{bmatrix} \psi_{ds} \\ \psi_{qs} \\ \psi_{0s} \\ \psi_{\mathrm{dr}} \\ \psi_{\mathrm{qr}} \\ \psi_{0r} \end{bmatrix} = \begin{bmatrix} L_s + L_{sr} & 0 & 0 & \frac{3}{2}M_{sr} & 0 & 0 \\ 0 & L_s + L_{sr} & 0 & 0 & \frac{3}{2}M_{sr} & 0 \\ 0 & 0 & L_s & 0 & 0 & 0 \\ \frac{3}{2}M_{sr} & 0 & 0 & L_r + L_{sr} & 0 & 0 \\ 0 & \frac{3}{2}M_{sr} & 0 & 0 & L_r + L_{sr} & 0 \\ 0 & 0 & 0 & 0 & 0 & L_{sr} \end{bmatrix} \begin{bmatrix} i_{ds} \\ i_{qs} \\ i_{0s} \\ i_{\mathrm{dr}} \\ i_{\mathrm{qr}} \\ i_{0r} \end{bmatrix}, \tag{3}$$

where L is the self-induction and M is the mutual induction.

2.2. Eccentric Magnetization Model of a Ceramic Motorized Spindle

2.2.1. Eccentricity Model of a Ceramic Motorized Spindle. The magnetic field density of the air gap is not only related to the material permeability but also has a direct relationship with the length of the air gap [25]. Due to the eccentricity of the stator and rotor, the length of the air gap is subject to a nonlinear variation rule. The eccentricity of the air gap is mainly caused by the rotor vibration in high-speed rotation. The air gap eccentricity and magnetic potential are shown in Figure 2.

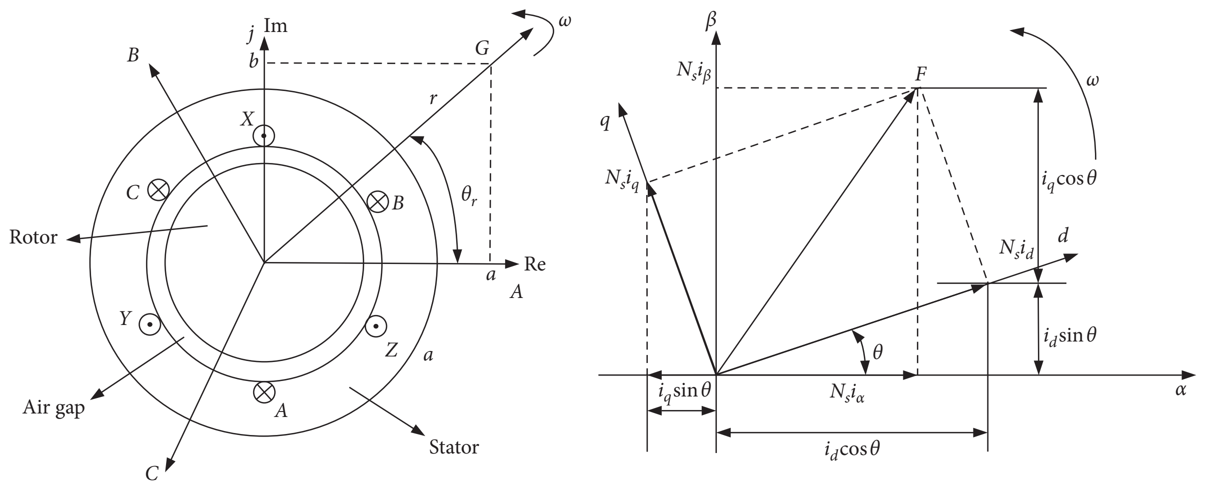

(a) (b)

Figure 1: The mechanism model of the motorized spindle: (a) the internal space vector of the motorized spindle; (b) vector diagram of magnetic space.

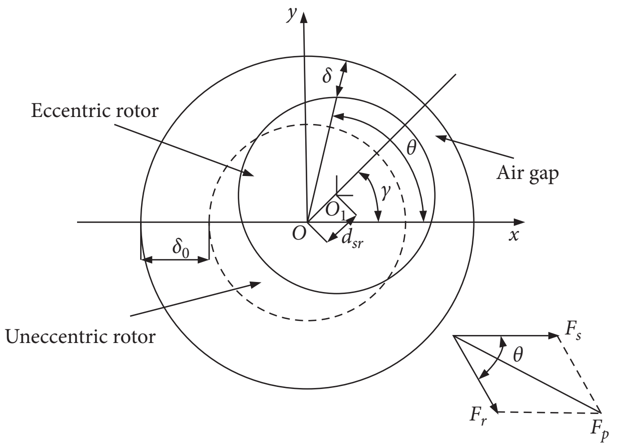

Figure 2: The air gap eccentricity and magnetic potential.

In the eccentric state, the relationship between the air gap and eccentric position is shown in the following equation [26]:

$$\delta = \delta_0 - d_{\mathrm{sr}} \cos(\theta - \gamma). \quad (4)$$

In the eccentric state, the element shape in the air gap is distorted. The Jacobi derivative method is used to calculate the unbalanced magnetic density in the eccentric state. The harmonic loss of the ceramic motorized spindle cannot be ignored. The eccentric air gap magnetic density of the stator and rotor is shown in the following equation [27]:

$$\begin{aligned} B_{\mathrm{air}}(\theta, t) = {} & \left(1 + \frac{\varepsilon}{2}\right) B_v \cos(p\theta - \omega_v t - \varphi_0) \\ & + 2\left(1 + \frac{\varepsilon}{2}\right) \sum_u B_u \cos(p\theta - \omega_u t - \varphi_u), \end{aligned} \quad (5)$$

where ε is the relative eccentricity, $\varepsilon = d_{\mathrm{sr}}/R_s - r_r$, v is the stator harmonic frequency, u is the rotor harmonic frequency, p is the pole logarithm of the motor, and φ_0 is the power factor angle.

Air gap magnetic common energy is a function of stator, rotor angle, and magnetic energy. It is directly related to the magnetic density of the motorized spindle, as shown in the following equation:

$$W_m = \frac{\mu_c}{2\mu_0} B_g^2 V = \frac{\mu_c \mu_0 \pi D l}{4\delta} \left(F_s^2 + F_r^2 + 2F_s F_r \cos\theta\right), \quad (6)$$

where D is the inner diameter of the stator, l is the effective length of the stator and rotor, θ is the angle between the stator and rotor magnetic potential, μ_0 is the permeability of the air gap, and μ_c is the permeability of ceramic.

2.2.2. Magnetization Model of a Motorized Ceramic Spindle.

Generally, the internal magnetic circuit of the motorized spindle is divided into five sections: stator yoke, stator tooth, air gap, rotor tooth, and rotor yoke. The rotating shaft is made of the ZrO_2 ceramic material. Rotor magnetization is mainly affected by rotational magnetization. The rotor yoke is affected by the ceramic reverse magnetic material, and the magnetic inductance line is distorted. There are magnetization alternating and magnetization rotating modes in the motorized spindle. The rotating magnetic field breaks down into two alternating magnetic fields, differing by 90 degrees, as shown in the following equation:

$$\phi = \sqrt{\phi_x^2 + \phi_y^2}. \quad (7)$$

The magnetization intensity of the ceramic motorized spindle rotor is orderly arranged by the magnetic moment of silicon molecules. The magnetic moment vector sum of all silicon molecules is shown in the following equation:

$$M = n \frac{\sum m + \sum \Delta m}{\Delta V} = \frac{j_m S \Delta l}{\Delta V}, \quad (8)$$

where $\triangle m$ is the additional magnetic moment of the molecule, m is the inherent magnetic moment of the molecule, $\triangle l$ is the stator and rotor contact length, S is the stator and rotor contact area, $\triangle V$ is the volume of magnetized medium, j_m is the current density of magnetized surface, and n is the number of molecules magnetized in a medium volume.

The magnetic field intensity of the ceramic rotating shaft is shown in the following equation:

$$H_{\mathrm{r}} = H_{\mathrm{ac}} + \alpha M = n i_{\mathrm{ac}} \sin(\omega t) + \alpha M, \tag{9}$$

where α is the curve parameters of ceramic magnetization ($\alpha < 1$) and H_{r} is the magnetic field intensity of the inner rotor domain.

A magnetization formula is obtained with the Langevin function, as shown in the following equation:

$$M_{\mathrm{an}} = M_{\mathrm{sa}}\left(\coth\frac{H_r + \alpha M_{\mathrm{an}}}{\alpha} - \frac{\alpha}{H_r + \alpha M_{\mathrm{an}}}\right). \tag{10}$$

According to the ampere loop theorem in ceramic and metal magnetic media, the magnetization relationship between B, M, and H is obtained as shown in the following equation:

$$\begin{aligned}\oint_L\left(\frac{1}{\mu_0}B_m - M_{\mathrm{an}}\right)\bullet \mathrm{d}r &= \oint_L\left(\frac{1}{\mu_0}\left(B_g + B_r\right) - M_{\mathrm{an}}\right)\bullet dr\\ &= \oint_L (H)\bullet \mathrm{d}r,\end{aligned} \tag{11}$$

where B_m is the magnetic medium density of the spindle.

2.2.3. Research on Electromagnetic Characteristics of a Ceramic Motorized Spindle. The influence of the complex motorized spindle electromagnetic characteristics is studied under different working conditions. The electromagnetic parameters of the motorized spindle eccentric magnetization model are calculated based on the ceramic reverse magnetic characteristics. The simulation condition is that the shaft material of 170SD30 ceramic motorized spindle is ZrO_2. The metal motorized spindle shaft material of the 170HT30 is 40Cr. The rotational speed was 9000 rpm, and the air gap was 0.3 mm. Under loading conditions, the speed difference was increased from 250 rpm to 1000 rpm, increasing by 250 rpm each time. Simulation results show the current and magnetic field density of the metal and ceramic motorized spindle changes under different working conditions. The changes in current under different working conditions are shown in Figure 3. The magnetic field density distribution of the spindle at different conditions is shown in Figure 4.

According to Figure 3(a), the metal and ceramic motorized spindles can be seen under the no-load condition, in which the current of the ceramic motorized spindle reaches 7.71 A and the metal motorized spindle reaches 9.36 A. The current of the metal motorized spindle is slightly higher than the ceramic motorized spindle. The main reason is the ZrO_2 shaft which has reverse magnetic properties. The magnetization moment generated by the rotor cannot make the large number of ceramic material molecules arranged in an orderly manner. The reverse magnetic properties of ceramics can effectively reduce the generation of induced current. At the same time, the alternating frequency of the magnetic field is higher. The distribution of magnetic flux density is not uniform due to the influence of eddy current. The magnetic flux is relatively large on the surface of the rotor. The skin effect on the metal motorized spindle current is obvious, which is the main reason that the current fluctuation of the metal motorized spindle is larger than the ceramic motorized spindle. Figure 3(b) shows that the motorized spindle current increases with the increase in air gap eccentricity. Because of the eccentricity of the air gap, the rotating flux of the stator and rotor is not uniform, which leads to the increase in current. Meanwhile, the current fluctuation with an air gap eccentricity of 0.2 mm is greater than that without eccentricity. The extreme value of 11.49 A in the eccentricity moment is more than 40% higher than the current without eccentricity. Due to the uneven distribution of the air gap, the rotation flux fluctuates violently. Air gap eccentricity changes the frequency of magnetic flux and produces different depths of skin eddy current. It has a direct influence on current fluctuation. Figure 3(c) shows that the motorized spindle current presents a rapid upward trend with the increase in the speed difference. When the loading slip ratio reaches 0.1111, the current reaches 55.875 A. When the spindle is running under a larger load, the stator and rotor current of the spindle will increase significantly. This will cause a sharp increase in leakage of the spindle magnetic field. The iron core of stator and rotor tooth positions is seriously saturated. The iron loss at the rotor tooth position of the spindle will increase under load, which makes the motor rotor current not only increase in amplitude but also increase in its fluctuation frequency.

The distribution diagram of rotor magnetic pole density is shown in Figure 4(a). It can be seen that the magnetic pole density of the ceramic motorized spindle rotor is smaller than the metal motorized spindle. The maximum magnetic pole of the metal motorized spindle rotor can reach 1.097 T. The maximum magnetic pole of the ceramic motorized spindle rotor is 50.1% lower than that of the metal motorized spindle. The ceramic shaft has reverse magnetic properties. Ceramic ZrO_2 molecules cannot be arranged in order. The magnetization phenomenon of the magnetic sensing line formed by the stator and rotor is weak. The material of the metal motorized spindle rotating shaft is 40Cr. The metal molecules are arranged in an orderly manner under the action of magnetic torque, and the magnetization phenomenon is obvious. Figure 4(b) shows the magnetic density distribution diagram about the middle position of the motorized spindle shell. Compared with Figures 4(b) and 4(a), the trend is consistent, though the magnetic density of the metal motorized spindle is higher than the ceramic motorized spindle. The magnetic density of the motorized spindle shell is much smaller than the rotor's magnetic pole. The maximum magnetic density of the metal motorized spindle shell is 15.598 μT. The maximum magnetic density of the ceramic motorized spindle shell is 10.094 μT. The main

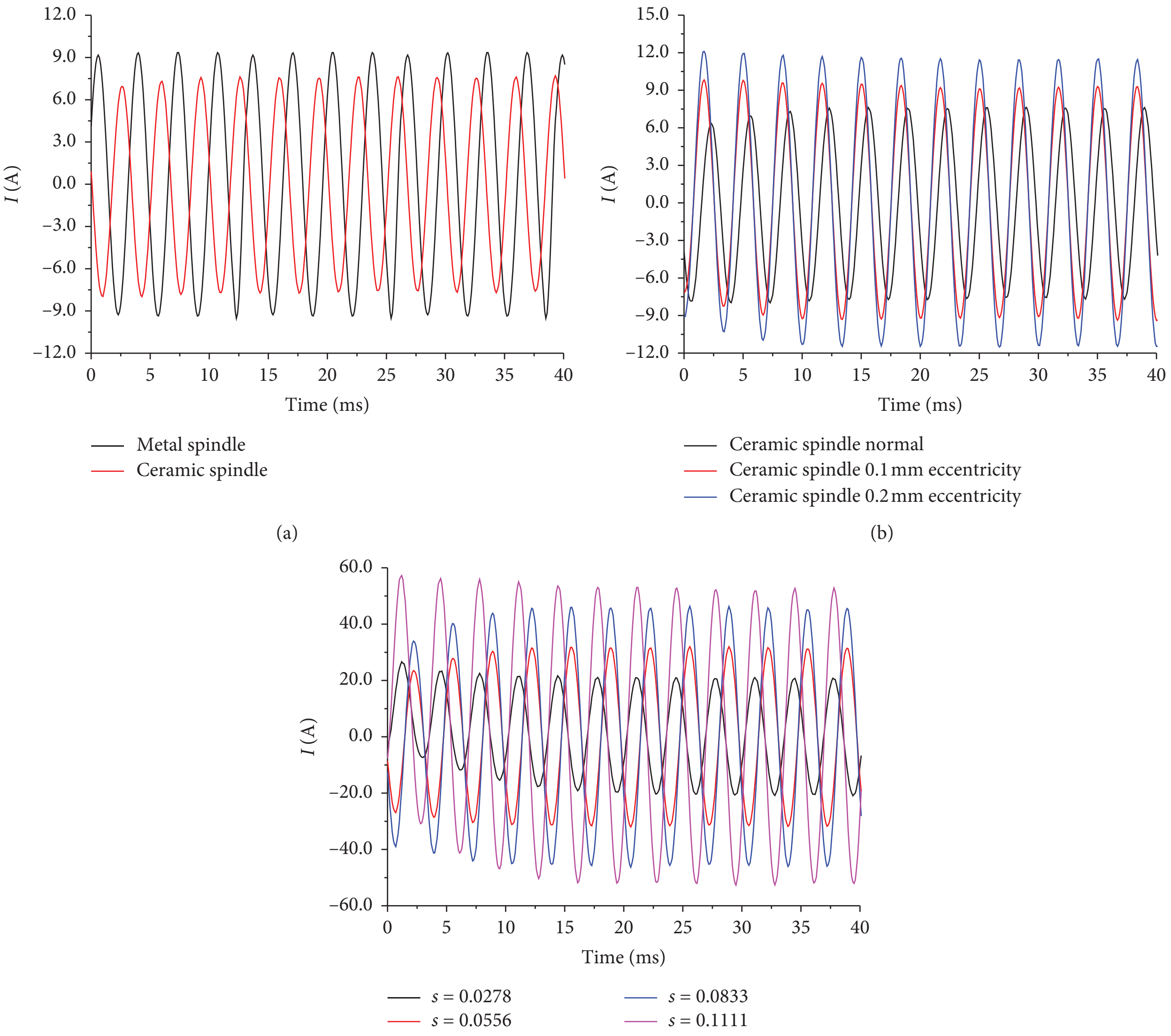

(a)

(b)

(c)

Figure 3: The current variation of the spindle at 9000 rpm: (a) no load current of metal, ceramic spindle; (b) no load current in air gap with different eccentricities of ceramic motorized spindle; (c) different load currents of ceramic motorized spindle.

reason is that the magnetic induction line is affected by the transmission distance in the transmission process. At the same time, the interference of the water channel, bearing housing, and other related parts is also the reason that the shell magnetic density is small. The distribution diagram of ceramic motorized spindle eccentric magnetic density is shown in Figure 4(c). Figure 4(c) shows that the maximum magnetic density of the air gap eccentricity of 0.1 mm is 0.749 T. Under the condition of 0.2 mm air gap eccentricity, the maximum magnetic density is 1.173 T, and the magnetic density alternating velocity is higher than the normal air gap magnetic density fluctuation. Due to the uneven distribution of air gap, the magnetic flux fluctuation is obvious. Especially in places with a small air gap, the alternating frequency of the magnetic field increases and the flux fluctuates dramatically, appearing like the phenomenon of magnetic density increases instantaneously.

Additionally, due to the ceramic reverse magnetic and the harmonic effect, the current and magnetic density of spindle is simulated through the magnetization model. In Figures 3 and 4, it is obvious that the magnetic and electric fields of ceramic spindle are smaller than those from metal spindle, which shows better adaptation for certain circumstances.

3. Loss Model of a Ceramic Motorized Spindle

The loss of a motorized spindle has a direct relationship with the thermal value of the spindle, which directly affects its thermal characteristics. The loss of a ceramic motorized spindle mainly includes mechanical loss and electromagnetic loss. Electromagnetic loss is directly related to alternating magnetization and rotational magnetization [28]. The establishment of a modified empirical coefficient model can

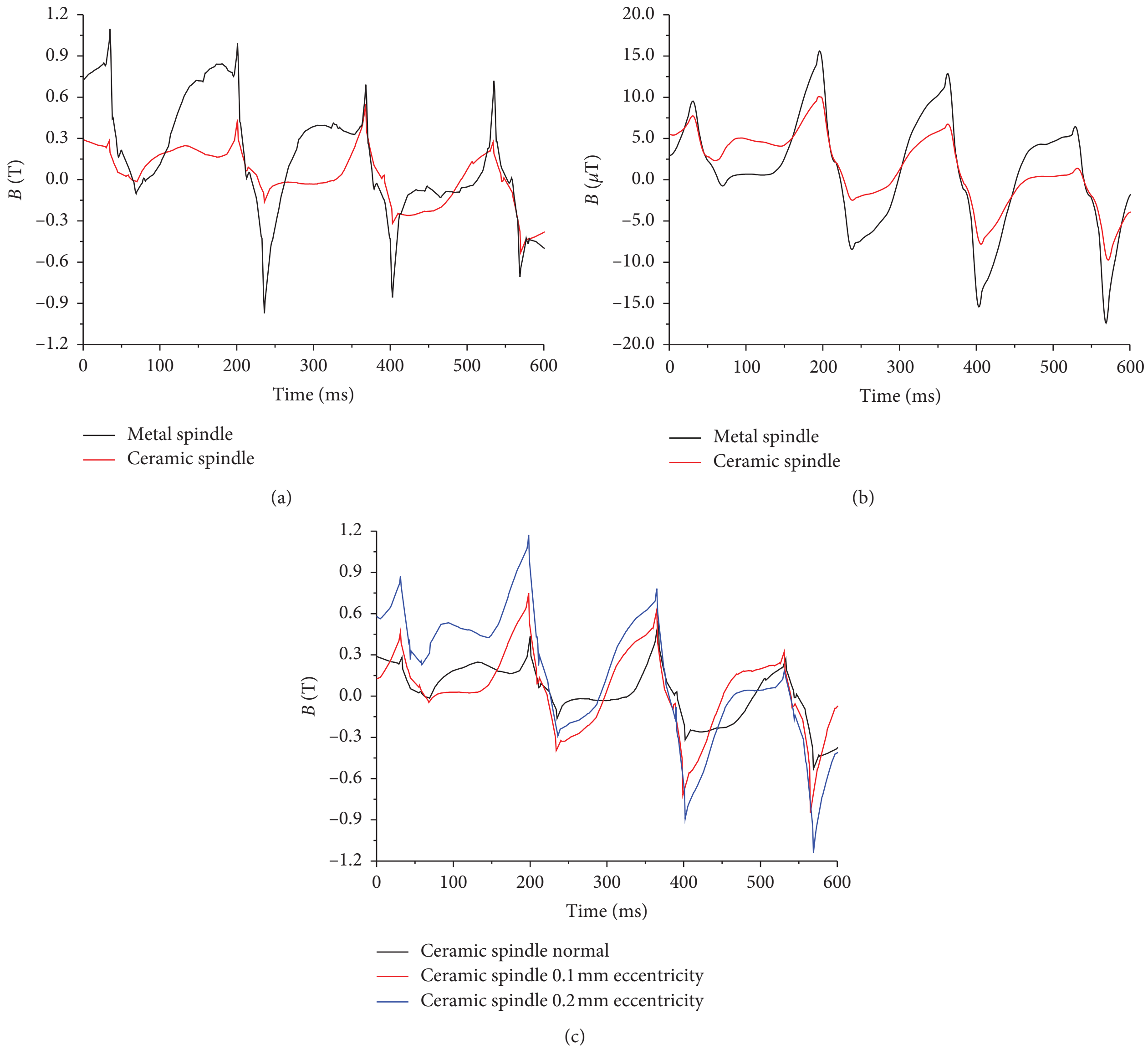

(a)

(b)

(c)

Figure 4: The magnetic field density distribution of a motorized spindle under different working conditions: (a) the distribution diagram of rotor magnetic pole density; (b) the magnetic density distribution about the middle position of the motorized spindle shell; (c) the distribution diagram of ceramic motorized spindle eccentric magnetic density.

improve the accuracy of predicting energy loss and efficiency under different working conditions.

3.1. Iron Consumption Model of a Ceramic Motorized Spindle. Iron loss is divided into hysteresis loss, eddy current loss, and abnormal loss. Hysteresis loss is accompanied by external magnetic field change. The rotor is made by silicon steel sheets. In a high-frequency alternating magnetic field, the skin effect is the main factor affecting the loss.

3.1.1. Hysteresis Loss. The fundamental reason for hysteresis loss is that the change in magnetic induction intensity lags behind the magnetic field intensity. The hysteresis of ceramic material is much smaller than the silicon steel material. The magnetic domain has a direct influence on the hysteresis loss mechanism. The magnetic domain distribution of ceramic and metal materials is shown in Figure 5.

Figure 5 shows the arrangement of the motorized spindle molecules at a random moment under the working condition of H magnetization intensity. When the external magnetic field M is applied to the ceramic material, only a few magnetic domain direction inside the ceramic materials can be arranged in order, and other molecules are arranged in disorder. The results show that only a few ceramic molecules in the magnetic domain change with the direction of magnetization. There is a weak relationship between the internal ceramic molecular structure and the external magnetic field. Under the action of external magnetic field M, there are many tiny spontaneous magnetization regions inside ferromagnetic materials. The molecules of silicon steel can be arranged in an orderly way. With the change in

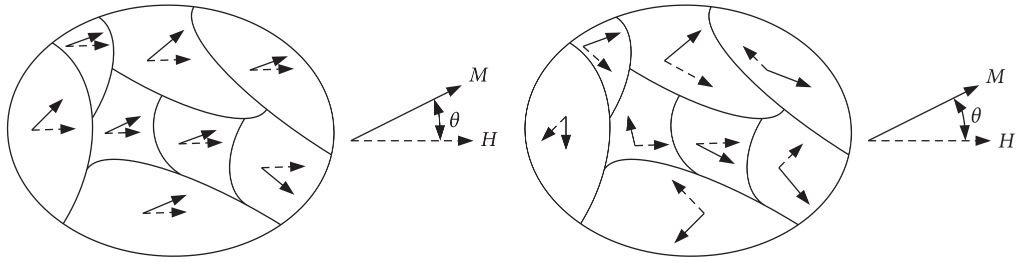

(a)

(b)

Figure 5: The magnetic domain distribution of ceramic and metal materials: (a) metal spindle; (b) ceramic spindle.

magnetization H inside the motorized spindle, most silicon steel molecules can achieve the same direction as the magnetization intensity M. A small number of silicon steel molecules cannot be quickly aligned with the M direction, which is mainly due to the intrinsic properties of ferromagnetic materials, magnetic crystal anisotropy interactions, and high-frequency magnetic field variation. It indicates that ferromagnetic materials have a direct influence on the external magnetic field, resulting in hysteresis of ferromagnetic materials. Hysteresis loss of the ceramic spindle is shown in the following equation:

$$P_h = k_h k_c f_n B_m^2 = k_h k_c \sum_j l_m A_j \left[\sum_n B_m^2 f_n\left(1 + k_{1v} B_m^{\beta_h}\right)\right], \tag{12}$$

where K_c is the hysteresis coefficient of ceramic ($K_c < 0.5$), l_{m} is the effective length of the stator and rotor, and A_j is the area of the j unit.

3.1.2. Loss of Eddy Current and Abnormal. A silicon steel rotor can induce an electromotive force in a high-frequency magnetic field. The electromotive force causes an eddy current in the closed rotor material. The eddy current is a circular current line induced in the silicon steel conductor and is one of the ceramic spindle main loss. The eddy current loss is directly related to the changing mode of the magnetic field and the permeability of the conductor. Reverse magnetic materials have less eddy current loss when rotating in an uneven magnetic field than paramagnetic materials. The molecules of ceramic materials cannot be arranged in large numbers, and induced eddy current generation can be effectively reduced so that large eddy current loss is avoided. The influence of magnetic domain movement on current is shown in Figure 6. According to the microscopic level of Figure 7, the eddy current loss generated by moving magnetization is analyzed. The amplitude of magnetic density produced by domain wall movement in silicon steel is twice that of the ceramic shaft.

Factors such as saturation, slot effect, and winding arrangement produce a large number of harmonics. A harmonic magnetic field leads to eddy current loss on the surface of the stator and rotor. A large number of voltage harmonics and higher harmonic voltage output by the frequency converter will have a great impact on the iron consumption of the spindle. The magnetic density in the iron core of the motorized spindle is distorted. The reverse magnetic effect of ceramic makes the magnetic density distribution of rotor tooth and yoke change, which also makes the harmonic magnetic field and the phenomenon of rotating magnetization change. During the rotation process of the ceramic motorized spindle, the magnetic intensity vector of the trajectory coordinate changes with the rotation θ angle. Eddy current loss of the magnetic density presents an elliptic shape. The v harmonic elliptic magnetic density diagram is shown in Figure 7.

The magnetization loss proportional coefficient of the ceramic motorized spindle is K_{a}. The density ellipticity of the ceramic motorized spindle δ is linearly related to the high-frequency harmonics. The hysteresis phenomenon of silicon steel sheet material is obvious and seriously affects the loss. The abnormal losses are shown in the following equation:

$$\begin{cases} \delta = \dfrac{B_{v\min}}{B_{v\max}}, \\ K_a = 1 + \delta, \\ P_a = K_a B^{1.5} f^{1.5} = K_a \sum\limits_j l_m A_j \sum\limits_n B_n^{1.5} f_n^{1.5}. \end{cases} \tag{13}$$

Influenced by the reverse magnetic effect of ceramic, the high-order loss coefficient of the harmonic eddy current K_{2v} is used to analyze the harmonic magnetic density of the rotor and the influence of rotor electrical density on spindle energy loss under different frequencies. The harmonic effect was considered. Bertotti's classical iron consumption model considered the eddy current loss and is shown in the following equation:

$$\begin{aligned} P_e &= k_e f_n^2\left(B_{v\max}^2 + B_{v\min}^2\right) \\ &= k_e \sum_j l_m A_j \left[\sum_n \left(\frac{B_n}{2}\right)^2 f_n^2 \left(1 + k_{2v} \frac{B_n^{\beta_e}}{2}\right)\right], \end{aligned} \tag{14}$$

where B_n is the magnitude of the n harmonic of the magnetic density through Fourier transform decomposition; K_e is the eddy current loss coefficient of silicon, $K_e = \pi^2 \gamma d^2/6\rho$; d is the length of silicon; ρ is the density of silicon; γ is conductivity; and β_e is the v harmonic additional eddy current loss coefficient of magnetic density.

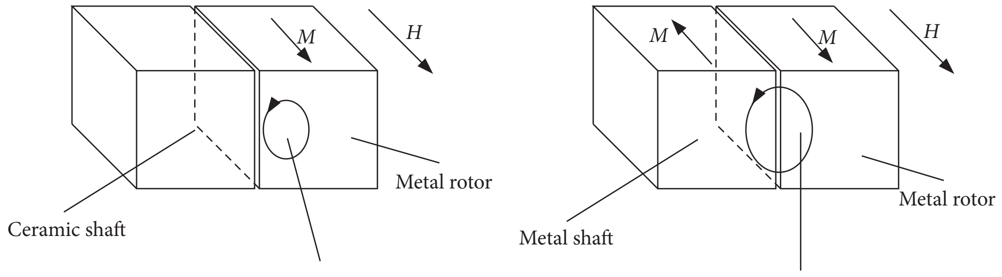

(a) (b)

Figure 6: The influence of magnetic domain movement on current: eddy current of (a) metal spindle and (b) ceramic spindle.

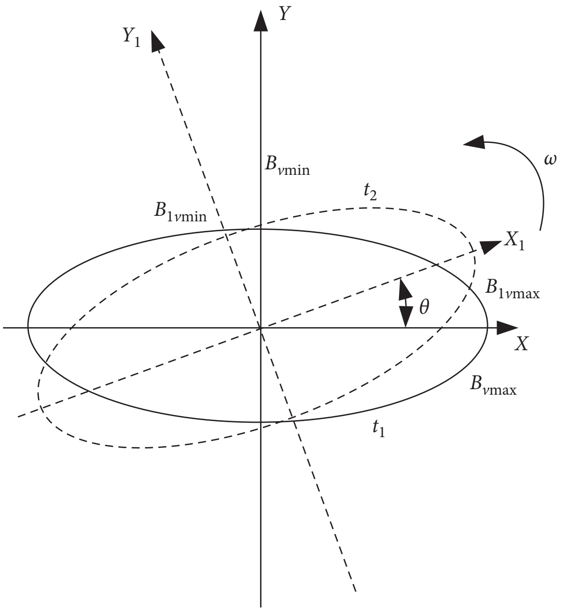

Figure 7: The v harmonic elliptic magnetic density diagram.

According to equations (12)–(14), the iron consumption of the ceramic motorized spindle can be obtained, as shown in the following equation:

$$\begin{aligned} P_{\mathrm{Fe}} &= k_h k_c \sum_j l_m A_j \left[\sum_n B_n^2 f_n \left(1 + k_{1v} B_n^{\beta_h} \right) \right] \\ &\quad + k_e \sum_j l_m A_j \left[\sum_n \left(\frac{B_n}{2} \right)^2 f_n^2 \left(1 + k_{2v} \frac{B_n^{\beta_e}}{2} \right) \right] \\ &\quad + K_a \sum_j l_m A_j \sum_n B_n^{1.5} f_n^{1.5}. \end{aligned} \tag{15}$$

3.2. Copper and Mechanical Loss of a Ceramic Motorized Spindle. Copper loss is an important part of the motorized spindle electromagnetic loss. The copper loss of a motorized spindle not only reduces the motor efficiency but also increases the temperature of the stator winding, which affects the motor's operation performance. According to Joule's law, the copper loss is the product of the stator winding current squared times the resistance. Stator current is mainly composed of excitation current and load current. The excitation current of I_{cu1} increases with the increase in rotating speed, while the load current of I_{cu2} decreases with the increase in rotating speed. According to the energy conduction law of a motorized spindle, there is a linear relationship between the ratio of excitation current and load current with the change in load. Therefore, the copper loss of the stator and rotor is shown in the following equation:

$$\begin{cases} I_{\mathrm{cu1}} + I_{\mathrm{cu2}} = I_{\mathrm{cu}}, \\ s = \dfrac{n_0 - n_1}{n_0}, \\ P_{\mathrm{cu}} = P_{\mathrm{cu}} + P_{v\mathrm{cu}} = 3 I_{\mathrm{cu}}^2 R_m \left(1 + K_v \right) + s P_{\mathrm{em}}, \end{cases} \tag{16}$$

where K_v is the resistance increasing coefficient of v harmonics ($K_v < 0.5$), s is the slip ratio, P_{em} is the electromagnetic power, n_0 is the preload speed, and n_1 is the load speed.

Mechanical loss is mainly composed of bearing friction loss and loss of ventilation. Bearing friction loss is directly related to bearing speed, the friction coefficient, the number of rolling bodies, and bearing load. Mechanical loss is shown in the following equation:

$$P_f = 0.15 \frac{F}{d} v \times 10^{-5} + 1.75 q v^2, \tag{17}$$

where P_f is the mechanical loss, F is the bearing load, d is the diameter of the ball, v is the rotation speed of the ball, and q is the air volume flow rate of the motorized spindle.

3.3. Loss Factors of a Ceramic Motorized Spindle. The influence of complicated ceramic motorized spindle loss was studied under different working conditions. The simulation condition is that the speed of 170SD30 ceramic motorized spindle is 9000 rpm. Calculation of the spindle loss model was based on ceramic reverse magnetic characteristics. Energy loss parameters, such as iron loss, copper loss, and output power, were calculated under no-load and different slip ratio loading conditions. The iron loss diagram of the ceramic motorized spindle under different working conditions is shown in Figure 8. The copper loss diagram is shown in Figure 9.

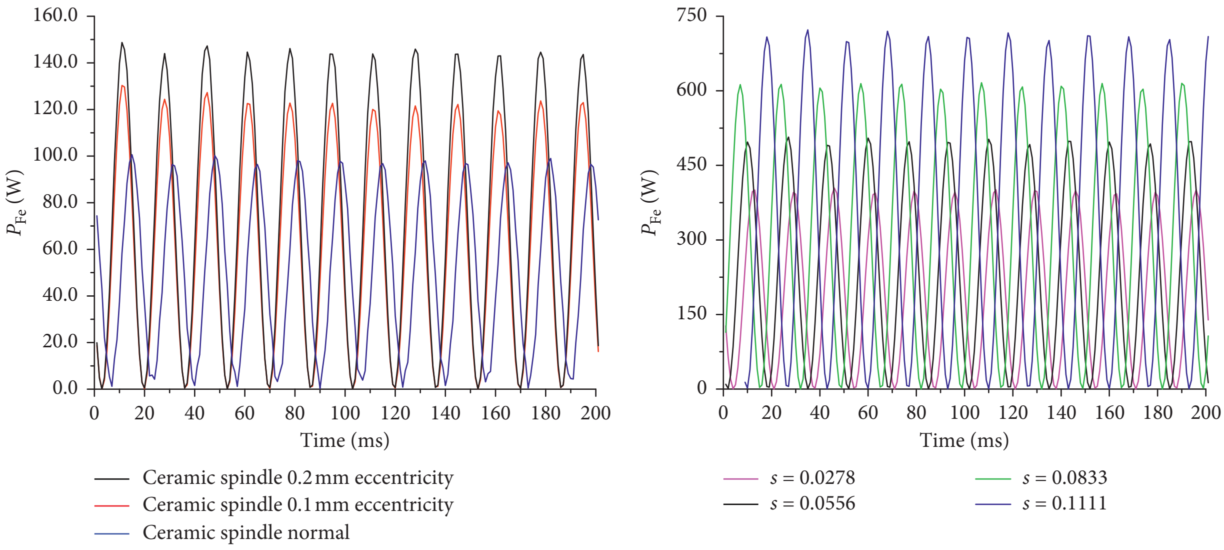

(a) (b)

Figure 8: Iron loss diagram of the ceramic motorized spindle under different working conditions: (a) eccentric iron loss of the ceramic motorized spindle; (b) speed difference of iron loss of the ceramic motorized spindle.

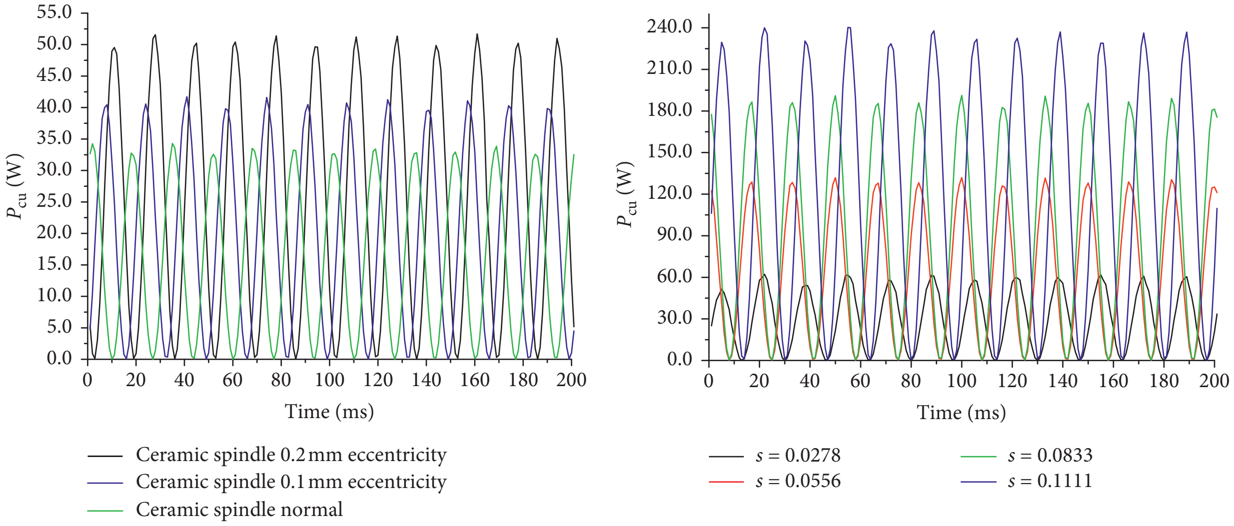

(a) (b)

Figure 9: Copper loss diagram of the ceramic motorized spindle under different working conditions: (a) the copper loss of the eccentric; (b) the copper loss of the speed difference.

It can be seen from Figure 8(a) that the ceramic motorized spindle loss is about 100 W under no eccentric load condition, which is less than the iron loss of the ceramic motorized spindle under eccentric working condition and only 2/3 of the iron loss of the 0.2 mm eccentric. The lower iron loss in the noneccentric working condition is due to the lower magnetization degree of the reverse magnetic material. The ceramic motorized spindle rotor's silicon steel is affected by the ceramic reverse magnetic property, which reduces the hysteresis iron loss and hysteresis degree of the rotor silicon steel material. Due to the eccentric air gap, the distribution of the air gap is uneven, and the smallest gap is only 0.1 mm. The magnetic flux alternating frequency increases. At the same time, the flux change has an obvious influence on the current skin effect. The iron loss also increases with the increase in the air gap unevenness. Figure 8(b) shows that the iron loss of the ceramic motorized spindle increases nonlinearly with the increase in the slip ratio. When the slip ratio reaches $s = 0.1111$, the iron consumption exceeds 700 W and is almost twice the slip ratio under the condition of $s = 0.0278$. This is mainly because the rotor current increases rapidly in the process of a large loading, in which the current exceeds 50 A in a short time. The magnetic domain wall experiences a jump rotation. The two domains appear as vibration through rubbing against each other, which leads to loss. The movement of the magnetic domain wall makes the eddy current distribution uneven. The eddy current and skin effects together cause the rotor magnetic flux density of the fluctuations. The induced voltage accumulates rapidly in the domain and produces a large loss.

Copper loss is mainly affected by Ohm's law. It can be seen from Figure 9 that the change rule of copper loss is similar to iron loss. With the increase in eccentricity and slip ratio, the copper loss and load will increase. This makes the spindle rotor current not only increase in amplitude but also increase in alternating current frequency due to the uneven width caused by eccentricity. The copper loss of the stator winding increases rapidly. By analyzing Figures 9(a) and 9(b), it can be seen that the maximum slip ratio $s = 0.1111$ reaches 240 W under loading conditions, which is much higher than under no-load and low-load conditions. The influence of the motorized spindle load on copper loss is greater than that of eccentricity. It also shows that the load has a more obvious influence on current.

According to equation (13), the friction and mechanical loss distribution diagram is obtained, as shown in Figure 10. There is a nonlinear relationship between the mechanical loss and the speed of the ceramic motorized spindle. In the process of the spindle rotating at medium and low speed, the mechanical loss has a relatively low impact on the loss of the spindle system. The loss of the bearing to the spindle during high-speed rotation cannot be ignored, and the mechanical loss exceeds 50 W under the condition that rotation speed is more than 2000 rpm. The friction between the ball and the outer ring channel generates heat. With the increase in bearing speed, the relation of generating heat square increases nonlinearly. It can also be seen from the figure that the mechanical loss of the metal motorized spindle is greater than the ceramic motorized spindle. This is mainly because of the self-lubricating properties, especially during high-speed rotation. Under the condition of constant oil supply, ceramic bearings have a more prominent lubrication effect and lower generation of heat. Ceramic bearings are characterized by high hardness and small deformation. The stiffness of the ball is not easy to soften in high-speed rotation. Compared to the contact area of the metal bearing channel, the ceramic is smaller. This is the reason that ceramic bearings generate less heat.

4. Experimental Verification and Analysis

4.1. Electromagnetic and Loss Experiments of a Ceramic Motorized Spindle. Oil and gas lubrication is adopted for spindle bearing lubrication under the test conditions. The experimental conditions are input oil of 5 mL/h, air pressure of 0.25 MPa, cooling water temperature of 289.15 K, and cooling water flow rate of 5 L/min. The speed is 9000 rpm, and the dragging loading test was carried out by another spindle. The loading range is from 9000 rpm to 8000 rpm, with speed increments of 200 rpm. A HIOKI FT3470-52 magnetic field tester and HIOKI MR8875-30 data acquisition instrument were used to conduct a magnetic density test of the spindle magnetic field for a 170SD30 ceramic spindle and 170HT30 metal spindle. A FLUCK NORMA 4000/5000 power analyzer was used to measure spindle current and harmonics. The measure of the magnetic field is shown in Figure 11, and the power analyzer measure of the ceramic motorized spindle is shown in Figure 12. The basic parameters of spindle are shown in Table 1, and the structural parameters of spindle are shown in Table 2.

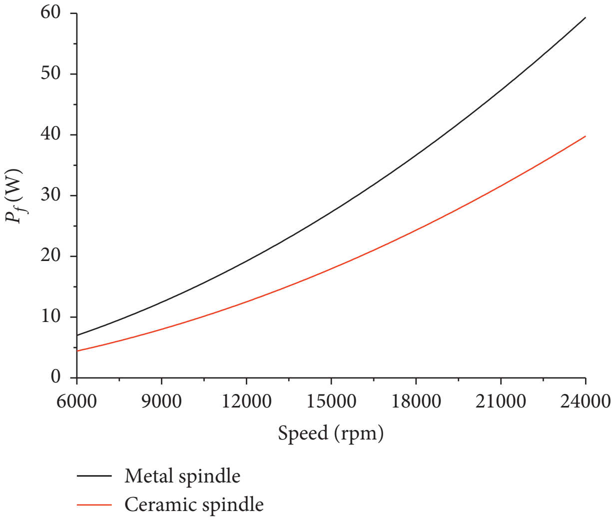

Figure 10: The friction and mechanical loss.

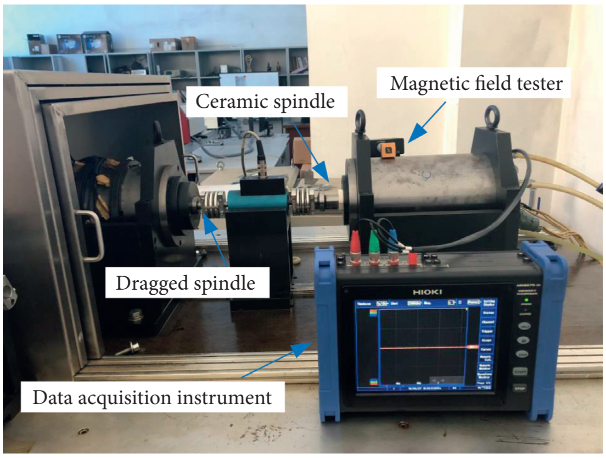

Figure 11: The measure of the magnetic field.

4.2. Experimental Results and Analysis. Magnetic field density was measured for the ceramic motorized spindle and metal motorized spindle shell. Magnetic density data were collected by using the HIOKI FT3470-52 magnetic field tester and HIOKI MR8875-30 data acquisition instrument. The magnetic density of spindle shell was measured under different load conditions; the comparison figure is shown in Figure 13. As can be seen from Figure 13(a), the magnetic density of the ceramic motorized spindle shell is smaller than the metal motorized spindle. The maximum magnetic density of the ceramic motorized spindle is only 9.946 μT, while for the metal motorized spindle is 16.37 μT. Figure 13(a) is comparable with Figure 5(b). The magnetic density error of the metal motorized spindle is 2.9%, while the ceramic motorized spindle magnetic density error is

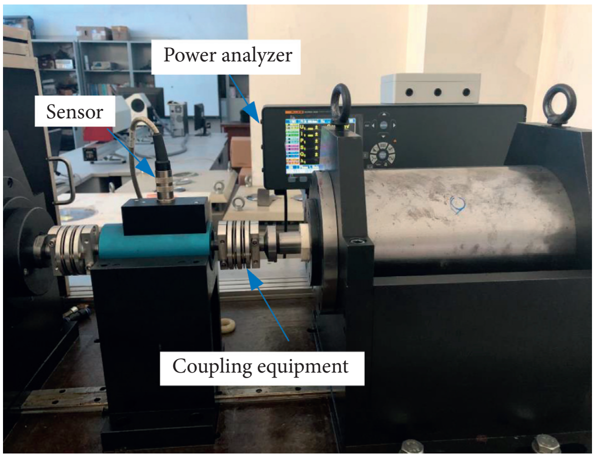

Figure 12: The power analyzer measure of the ceramic motorized spindle.

Table 1: The basic parameters of spindle.

The basic parameters of spindle	170SD30 ceramic spindle	170HT30 metal spindle
Rated speed (rpm)	30000	30000
Rated voltage (V)	350	350
Pole logarithm	4	4
Shaft material	ZrO_2 ceramic	40Cr steel
Power (Kw)	15	15
Torque (Nm)	5	5

Table 2: The structural parameters of spindle.

Stator and rotor		
1	The outer diameter of rotor (mm)	79.4
2	The inner diameter of stator (mm)	80
3	The coil span of stator (mm)	63.095
4	The outer diameter of stator (mm)	130
5	The turns of stator winding, n	6
6	The coil pitch, d (mm)	5

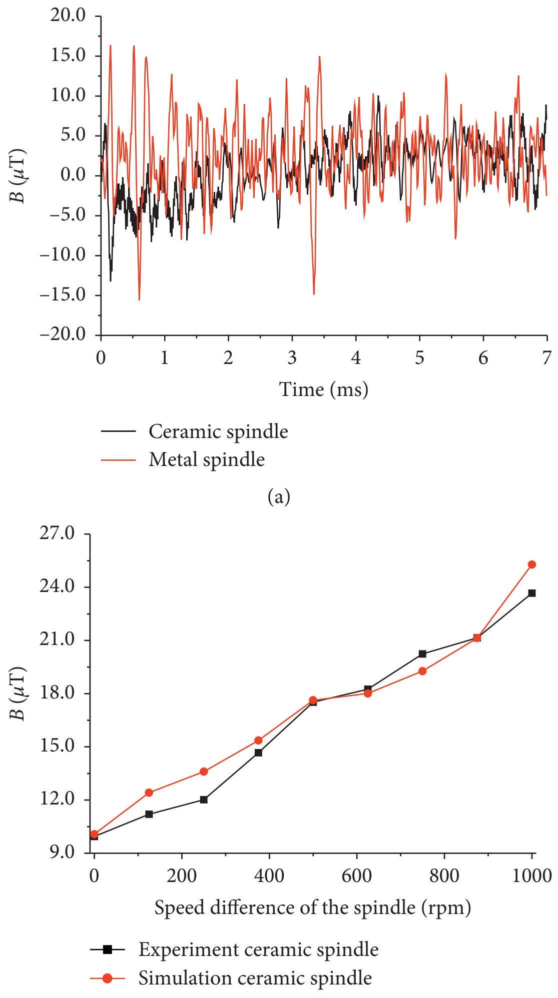

(a)

(b)

Figure 13: The magnetic density of the spindle shell measured under different load conditions: (a) ceramic, metal spindle magnetic density experiment under no-load conditions; (b) the magnetic density of different speed differences under 9000 rpm.

1.89%. The magnetization model can be precisely verified through the comparisons with different spindles. Figure 13(b) is the comparison diagram of magnetic density simulation and experiment under different loading conditions. It can be seen that different loads are loaded at the operating condition of 9000 rpm. Magnetic density and loading show a nonlinear increasing relationship. The maximum magnetic density error of the motorized spindle shell in simulation and testing is 2.14 μT. The magnetic density distribution of the shell can also reflect the magnetic density distribution change in the rotor pole.

The harmonic frequency domain, current, and power of the motorized spindle were obtained using the FLUCK NORMA 4000/5000 power analyzer. The harmonic frequency domain and current of the motorized spindle are shown in Figure 14. The relationship between spindle loss and torque load is shown in Figure 15. Figure 14(a) analyzes the harmonic spectrum of the current under the condition of a motorized spindle at 9000 rpm, for which the speed difference is 400 rpm. The energy of the spindle in the low-frequency region is greater than that in the middle and high-frequency regions. It can be concluded that the reverse magnetic properties of ceramic can effectively reduce the influence of harmonics on current compared with the metal paramagnetic properties. Figure 14(b) shows that, in the simulation calculation considering harmonics, the average error of 1.91% is in good agreement with the current value measured in the experiment. The simulation current without considering harmonics is smaller than the experimental current, with an average error of 9.43%. The current error was as high as 16.7% under some large load conditions. It is shown that harmonics are an important factor, affecting the fluctuation and magnitude of current.

The input and output power of the ceramic motorized spindle can be measured through a power analyzer. Figure 15(a) shows the relationship between input power, torque, and the speed difference of the motorized spindle. In the figure, it can be seen that the input power exhibits a

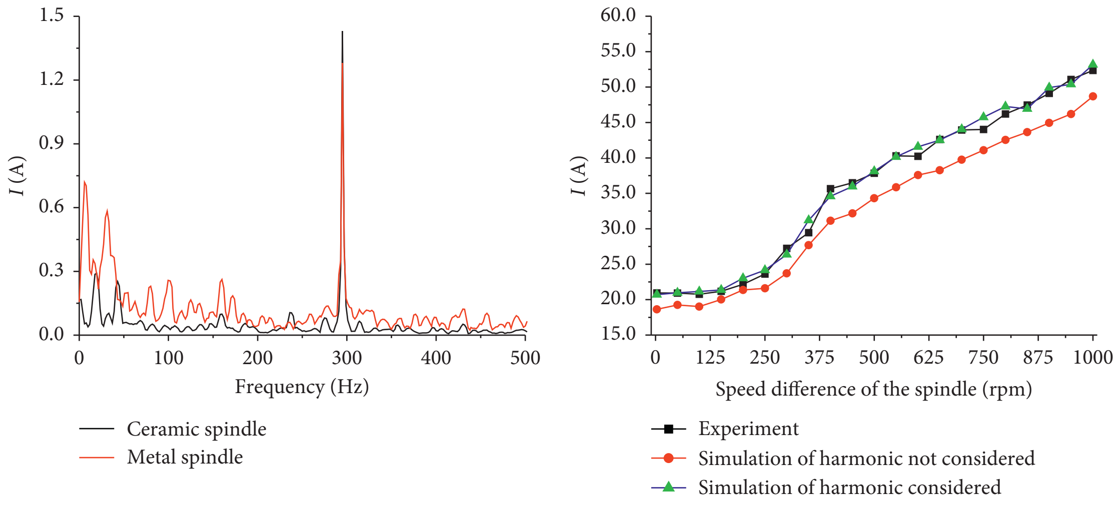

(a) (b)

Figure 14: The current of a ceramic motorized spindle: (a) the current harmonic frequency of ceramic and metal motorized spindles; (b) comparison of experimental and simulated current.

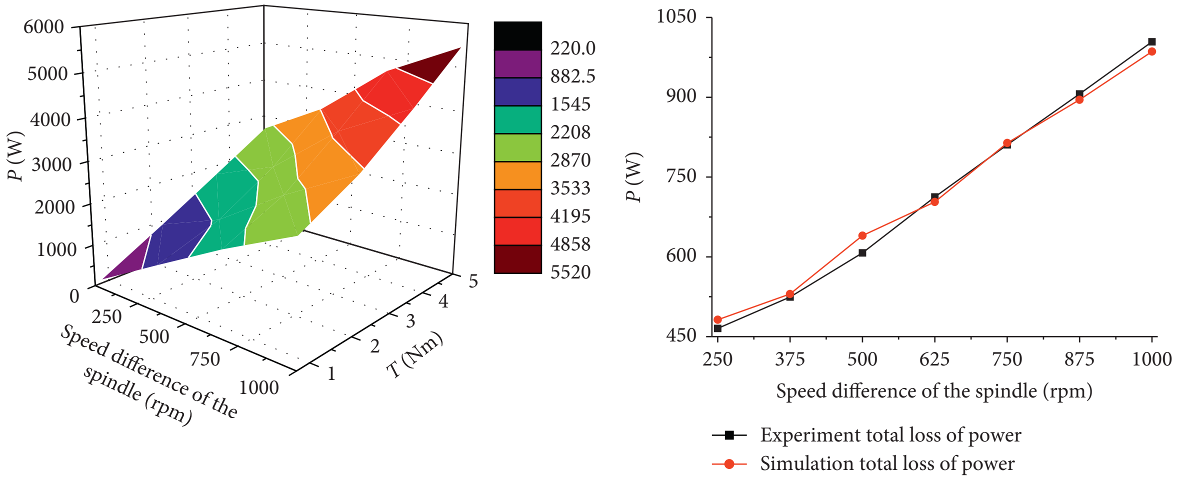

(a) (b)

Figure 15: Comparison of the relationship between loss and speed difference: (a) the relationship between input power, torque, and speed difference of a motorized spindle; (b) the loss comparison of simulation and experiment.

nonlinear increasing relationship with the increase in speed difference and torque. Under a low-load condition, torque increases rapidly, while under middle load conditions, torque and input power increase slowly. Under the condition that the rotation speed difference reaches 1000 rpm, the input power reaches the maximum value of 5505 W. Figure 15(b) shows the ceramic motorized spindle variation diagram of the total loss under different loading conditions. At the speed difference of 500 rpm, the maximum power difference is 32.47 W, the total simulation loss is 639.84 W, and the total loss of the experiment is 607.37 W.

The existing simulation model for spindle loss is usually larger than reality. And the simulation accuracy can be obviously improved by considering the characteristics of ceramic reverse magnetism and the harmonic effect. The proposed spindle loss model simulating the maximum loss error is 5.07% and the average error is 2.1%. It is meaningful to develop a new electromagnetic spindle loss mechanism model to simulate the complex conditions.

5. Conclusions

An electromagnetic loss model of a ceramic motorized spindle considering the reverse magnetic effect is proposed. This model can be used to analyze the influence of parameters, such as current, magnetic density, and loss under different working conditions. The influence of harmonics, reverse magnetic characteristics, and eccentricity on the ceramic motorized spindle magnetic field is analyzed. In addition, the influence of different loads on the ceramic motorized spindle copper and iron and the mechanical loss is studied. The conclusions are as follows:

(1) The electromagnetic physical model of a spindle system was studied. The magnetization eccentricity model of a ceramic motorized spindle was established by combining the Park formula and the Jiles–Atherton theory. The magnetic density of a ceramic motorized spindle at different conditions was simulated. Air gap eccentricity and magnetic density showed a nonlinear increasing relationship. The air gap magnetic density of a ceramic motorized spindle was obviously affected by the reverse magnetic effect. The air gap magnetic density of ceramic motorized spindle was only 64.7% of metal motorized spindle.

(2) Considering the magnetization model of the reverse magnetic effect, the ceramic motorized spindle's current and loss were smaller than the metal motorized spindle. Due to the hysteresis and eddy current, the loss mechanism of the ceramic motorized spindle was changed by the ceramic reverse magnetic property.

(3) The loss model of the ceramic motorized spindle was calculated by Ohm's law. Combined with Bertotti's classical iron loss model, the influence of a ceramic bearing on the ceramic motorized spindle mechanical loss was considered. The distribution of loss under different load conditions was studied. The loss of the ceramic motorized spindle increased nonlinearly with the increase in load. Compared with the experimental results, the average loss error was 2.1%. The electromagnetic model of a ceramic motorized spindle has high accuracy.

Nomenclature

ω: Angular velocity rotation
N_s: The number of winding circle
i: Current
ψ: Flux linkage
R: Resistance
p: Differential operator
u: Voltage
δ: Air gap eccentricity
γ: Offset angle of rotor
θ: Rotation angle of rotor
d_{sr}: The eccentricity of the distance
B: Magnetic density
V: The volume of air gap
F: Potential energy of magnetic field
W: Synthetic potential energy
Φ: Magnetic flux
M: Magnetization intensity
H: Magnetic field intensity vector
K: Loss coefficient of hysteresis
β: Additional coefficient of magnetic density
δ: Ovality
μ_0: Air permeability
f: Frequency
P: Loss power

Subscript

d: d-axis
q: q-axis
s: Stator
r: Rotor
sr: Stator and rotor
ds: Stator equivalent on the d axis
qs: Stator equivalent on the q axis
dr: Rotor equivalent on the d axis
qr: Rotor equivalent on the q axis
ac: Alternating current
an: No hysteresis
sa: Saturation
g: Air gap
ap: Preload of bearing
a: Abnormal loss coefficient
e: Eddy current loss
$1v$: Additional low-order coefficient of harmonic hysteresis loss
h: Hysteresis loss
$v_{\min}$: Elliptic short axis of V harmonic magnetic density
$v_{\max}$: Elliptic long axis of V harmonic magnetic density
cu: Equivalent copper loss
$2v$: Higher order eddy current loss coefficient of v harmonic.

Data Availability

The data used to support the findings of this study are available from the corresponding author upon request.

Conflicts of Interest

The authors declare that they have no conflicts of interest.

Acknowledgments

This work was funded by the National Natural Science Foundation of China (Grant no. 51675353) and the innovation team project about the Ministry of Education of China (Grant no. IRT-15R45).

References

[1] H. T. Shi and X. T. Bai, "Model-based uneven loading condition monitoring of full ceramic ball bearings in starved lubrication," *Mechanical Systems and Signal Processing*, vol. 139, Article ID 106583, 2020.
[2] L. Gu and Y. Shi, "Online monitoring technique of power condition for inverter-fed motor driven hydraulic system," *Mathematical Problems in Engineering*, vol. 2019, Article ID 4908942, 16 pages, 2019.
[3] P. Alkorta, O. Barambones, A. Zubizarreta, and J. A. Cortajarena, "Effective and robust generalized predictive speed control of induction motor," *Mathematical Problems in Engineering*, vol. 2013, Article ID 913458, 14 pages, 2013.
[4] D. Ma, X. Hu, H. Zhang, Q. Sun, and X. Xie, "A hierarchical event detection method based on spectral theory of multidimensional matrix for power system," *IEEE Transactions on Systems, Man, and Cybernetics: Systems*, vol. 9, pp. 1–14, 2019.

[5] H. Zhang, Y. Li, D. W. Gao, and J. Zhou, "Distributed optimal energy management for energy internet," *IEEE Transactions on Industrial Informatics*, vol. 13, no. 6, pp. 3081–3097, 2017.

[6] Y. Li, H. Zhang, X. Liang, and B. Huang, "Event-triggered-based distributed cooperative energy management for multienergy systems," *IEEE Transactions on Industrial Informatics*, vol. 15, no. 4, pp. 2008–2022, 2019.

[7] Y. Li, H. Zhang, B. Huang, and J. Han, "A distributed Newton–Raphson-based coordination algorithm for multi-agent optimization with discrete-time communication," *Neural Computing and Applications*, vol. 10, pp. 1–15, 2018.

[8] M. P. Sruthi, C. Nagamani, and G. Saravana Ilango, "An improved algorithm for direct computation of optimal voltage and frequency for induction motors," *Engineering Science and Technology, an International Journal*, vol. 20, no. 5, pp. 1439–1449, 2017.

[9] A. P. F. Machado, C. Z. Resende, and D. C. Cavalieri, "Estimation and prediction of motor load torque applied to electrical submersible pumps," *Control Engineering Practice*, vol. 84, pp. 284–296, 2019.

[10] F. R. Ismagilov, I. K. Khairullin, V. E. Vavilov, V. I. Bekuzin, A. S. Karimov, and R. D. Karimov, "Energy losses in the electric motor of a high-speed spindle," *Russian Engineering Research*, vol. 37, no. 3, pp. 253–257, 2017.

[11] R. Wang, Q. Sun, D. Ma, and Z. Liu, "The small-signal stability analysis of the droop-controlled converter in electromagnetic timescale," *IEEE Transactions on Sustainable Energy*, vol. 10, no. 3, pp. 1459–1469, 2019.

[12] J. Asama, R. Kawata, T. Tamura, T. Oiwa, and A. Chiba, "Reduction of force interference and performance improvement of a consequent-pole bearingless motor," *Precision Engineering*, vol. 36, no. 1, pp. 10–18, 2012.

[13] A. Dalcali and M. Akbaba, "Comparison of 2D and 3D magnetic field analysis of single-phase shaded pole induction motors," *Engineering Science and Technology, an International Journal*, vol. 19, no. 1, pp. 1–7, 2016.

[14] P. Liu, F. Liu, and H. Qiu, "A novel approach for acquiring the real-time energy efficiency of machine tools," *Energy*, vol. 121, pp. 524–532, 2017.

[15] V. Petrushin, B. Bendahmane, B. Yahiaoui, and A. Yakimets, "Influence of magnetic circuit saturation and skin effects on the adjustable induction motor characteristics," *International Journal of Hydrogen Energy*, vol. 42, no. 48, pp. 29006–29013, 2017.

[16] A. Guha and G. Narayanan, "Small-signal stability analysis of an open-loop induction motor drive including the effect of inverter dead-time," *IEEE Transactions on Industry Applications*, vol. 52, no. 1, pp. 1–6, 2016.

[17] A. Akbari, M. Danesh, and K. Khalili, "A method based on spindle motor current harmonic distortion measurements for tool wear monitoring," *Journal of the Brazilian Society of Mechanical Sciences and Engineering*, vol. 39, no. 12, pp. 5049–5055, 2017.

[18] C. Li, J. Xing, and L. Xu, "Coupled vibration of driving sections for an electromechanical integrated harmonic piezodrive system," *AIP Advances*, vol. 4, no. 3, pp. 1–9, 2014.

[19] K. Wang, R. Huai, Z. Yu, X. Zhang, F. Li, and L. Zhang, "Comparison study of induction motor models considering iron loss for electric drives," *Energies*, vol. 12, no. 3, pp. 1–13, 2019.

[20] J. Wójcicki and G. Bianchi, "Electric load management in spindle run-up and run-down for multi-spindle machine tools via optimal power-torque trajectories and peak load synchronization," *The International Journal of Advanced Manufacturing Technology*, vol. 95, no. 5–8, pp. 1819–1835, 2018.

[21] P. Hao, M. Cheng, R. Cao, Y. Wang, and Z. Wang, "Research on induction motor energy saving strategy using voltage regulation control," *International Conference on Electrical Machines & Systems*, vol. 12, pp. 1–6, 2010.

[22] E. C. Bortoni, J. V. Bernardes, P. V. V. Da Silva, V. A. D. Faria, and P. A. V. Vieira, "Evaluation of manufacturers strategies to obtain high-efficient induction motors," *Sustainable Energy Technologies and Assessments*, vol. 31, pp. 221–227, 2019.

[23] Y. H. Kim, B. C. Cheon, and J. H. Lee, "Design of spoke type motor and magnetizer for improving efficiency based rare-earth-free permanent-magnet motor," *AIP Advances*, vol. 8, no. 5, pp. 1–6, 2018.

[24] T. Vihekar, M. Ballal, and H. Suryawanshi, "Application of multiple parks vector approach for detection of multiple faults in induction motors," *Journal of Power Electronics*, vol. 17, no. 4, pp. 972–982, 2017.

[25] H. Shi, N. Niguchi, and K. Hirata, "Analytical calculation of air gap magnetic field distribution in magnetic geared motors," *Journal of Power Electronics*, vol. 19, no. 3, pp. 794–802, 2019.

[26] W. Huang and C. Gan, "Bifurcation analysis and vibration signal identification for a motorized spindle with random uncertainty," *International Journal of Bifurcation and Chaos*, vol. 29, no. 1, pp. 1–17, 2019.

[27] K. Zhang, Z. Wang, H. Shi, X. Bai, and Z. Wang, "Research on vibration characteristics of a ceramic spindle based on the reverse magnetic effect," *Shock and Vibration*, vol. 2019, Article ID 6934087, 15 pages, 2019.

[28] H. Park, S. Park, D. Kim, and J. Kim, "Hybrid phase excitation method for improving efficiency of 7-phase BLDC motors for ship propulsion systems," *Journal of Power Electronics*, vol. 19, no. 3, pp. 761–770, 2019.